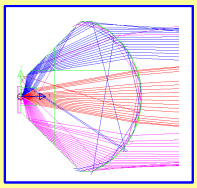

Ventura Photonics

Photonics Solutions

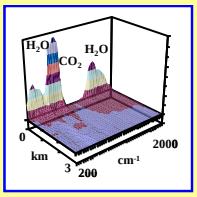

Missing the Heat Transfer

Roy Clark PhD

Ventura Photonics Climate Note 6, VPCN 006.1
Ventura Photonics
Thousand Oaks, CA
October 2019

Simple comparison of climate model temperature predictions with observations shows that the models have consistently predicted higher temperatures than those measured. This difference is sometimes called the missing heat. In reality, the climate models have failed. This is illustrated in Figure 1. The reason for this failure is that the models are missing key elements of the surface heat transfer. In particular, the coupling of the LWIR flux to the wind driven evaporation at the ocean surface has been ignored. In addition, the vertical transport associated with the ocean gyre circulation has also been neglected. Surface heat transfer has been discussed in more detail by Clark [2019a, b, c, d, e, 2013a, b, 2011]

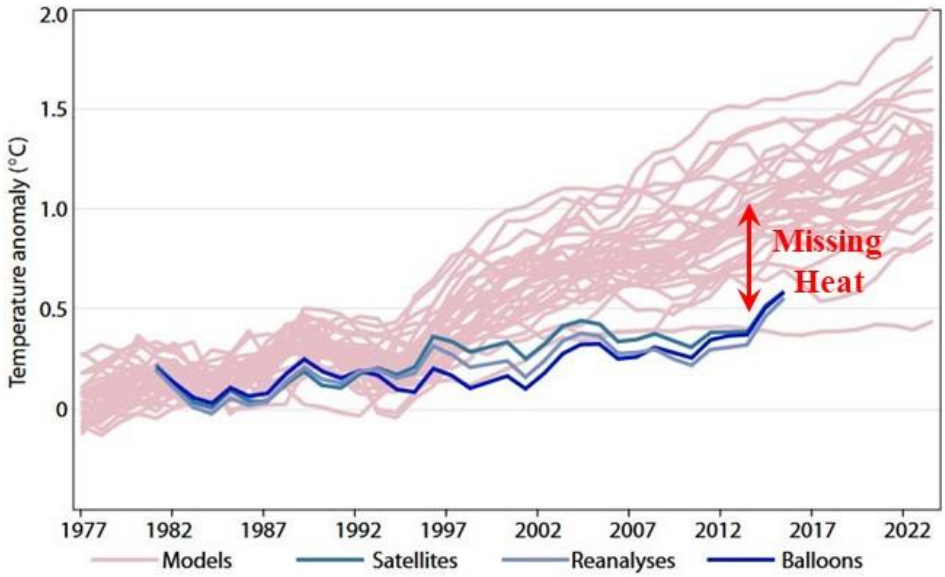

Figure 1: Tropical mid-tropospheric temperatures, models vs. observations. Models in pink, against various observational data sets in shades of blue. Five year averages, 1979-2017. Trend lines cross zero at 1979 for all series [Christie, 2019].

Over the last 200 years, the atmospheric concentration of CO_2 has increased by 120 parts per million (ppm) from 280 to 400 ppm. This has produced an increase in the downward long wave IR (LWIR) flux from the atmosphere to the Earth's surface of approximately 2 W m^{-2}. Straightforward time dependent analysis of the surface heat transfer shows that the increase in surface temperature resulting from this increase in LWIR flux is too small to measure [Clark, 2019a, 2019b]. The penetration depth of the LWIR flux into the ocean is approximately 100 micron. Within this layer, the LWIR flux is fully mixed with the wind driven evaporative flux. The small increase in flux from CO_2 cannot couple below this layer and produce any measurable change in ocean temperature. The penetration depth of LWIR radiation into water for 99% attenuation is shown in Figure 2 [Hale & Querry, 1972].

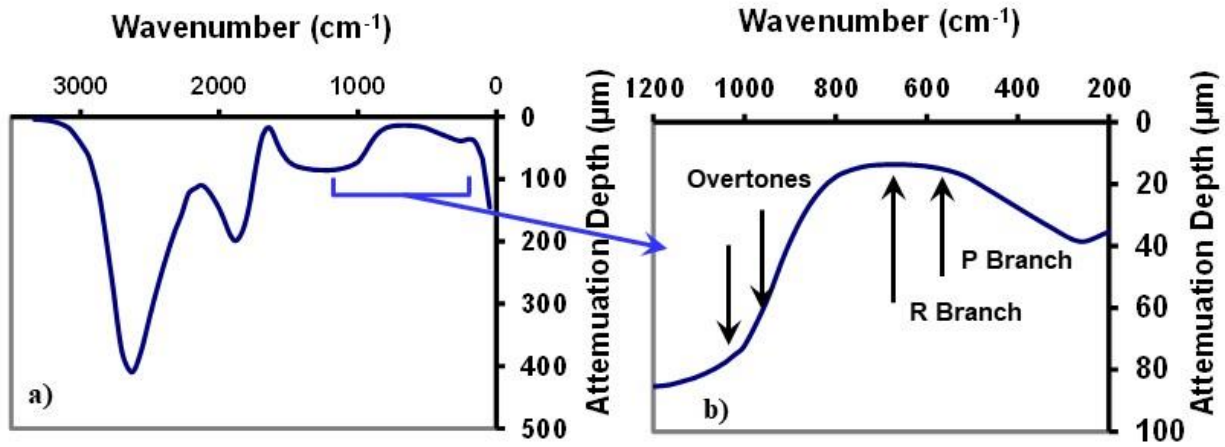

Figure 2: The penetration depth of the LWIR flux into water (for 99% attenuation). a) 3300 to 50 cm^{-1} and b) water 1200 to 200 cm^{-1}. The spectral location of the CO_2 emission band increases are indicated.

The ocean surface is almost fully transparent to the incident solar flux. Approximately half is absorbed within the first 1 m layer of the ocean and 90% is absorbed within the first 10 m layer. The absorption of the solar flux vs. depth is shown in Figure 3. When diurnal mixing and wave action is included, the absorbed solar heat is initially distributed within the first 100 m layer of the ocean. At the surface, the thermal gradient at the ocean-air interface is small, typically 1 C. This means that the ocean surface must warm up until the absorbed solar heat can be removed by a combination of net LWIR flux and wind driven evaporation. The cooler water produced at the surface then sinks and cools the bulk ocean layers below. It is replaced by upwelling warm water. This is a Rayleigh-Benard type of convection with columns of water moving in opposite directions. It is not a simple diffusion process. This convection cycle continues to provide heat to the surface at night, so the wind driven evaporation continues at night. The thermal storage is not localized and heat can be transported and recirculated over very long distances.

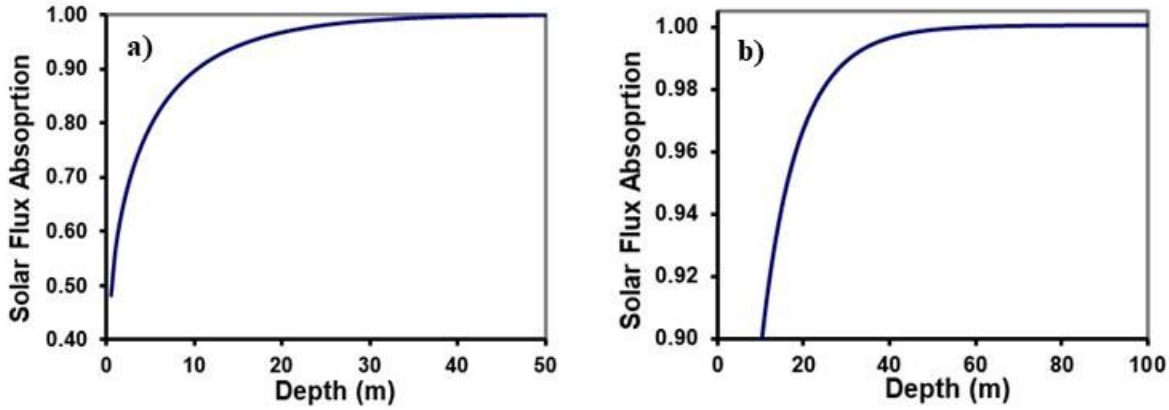

Figure 3: Ocean attenuation of the solar flux vs. depth a) to 50 m depth, b) enlarged scale to 100 m depth.

Convection is amass transport process that is coupled to the rotation or angular momentum of the earth. This produces the characteristic Hadley, Ferrell and Polar cell convective structure and the trade winds that drive the ocean gyre circulation [UK Met Office, 2017]. There can never be an exact flux balance between the wind driven evaporation and the solar heating. This means that various quasi-periodic ocean oscillations are established. The three main ones are the Pacific Decadal Oscillation (PDO), the Atlantic Multi-decadal Oscillation (AMO) and the El Nino Southern Oscillation (ENSO). All of these have major impacts on the earth's climate and their effects can be seen in the climate record. The AMO and PDO have periods of oscillation near 60 years. The ENSO is a short term oscillation with a period between 3 and 7 years. It involves changes in the size and location of the Pacific warm pool and is caused by variations in wind speed over the equatorial Pacific Ocean. As the wind speed decreases, the residence time in the gyre circulation near the equator increases and the evaporation decreases. Both of these lead to an increase in surface temperature. There are various measures of the ENSO index and the wind speed. Figure 4a shows the ENSO index developed by the Japanese Meteorological Agency (JMA) and the Southern Oscillation Index (SOI) from the Australian BOM [ENSO 2019, SOI 2019]. The JMA ENSO index based on the average temperature in the equatorial Pacific Ocean from 4° N to -4° S and from 90° to 150° W. The SOI is the pressure difference between Tahiti and Darwin. There is an inverse relationship between temperature and pressure, since the wind speed increases with the pressure difference. For clarity, SOI index is plotted with the sign reversed. The indices are both related to changes in flow rate in the tropical S. Pacific gyre. The cumulative ENSO index from 1880 (the sum over time) is shown in Figure 4b. The cooling from 1940 to 1980 and the subsequent warming can be clearly seen.

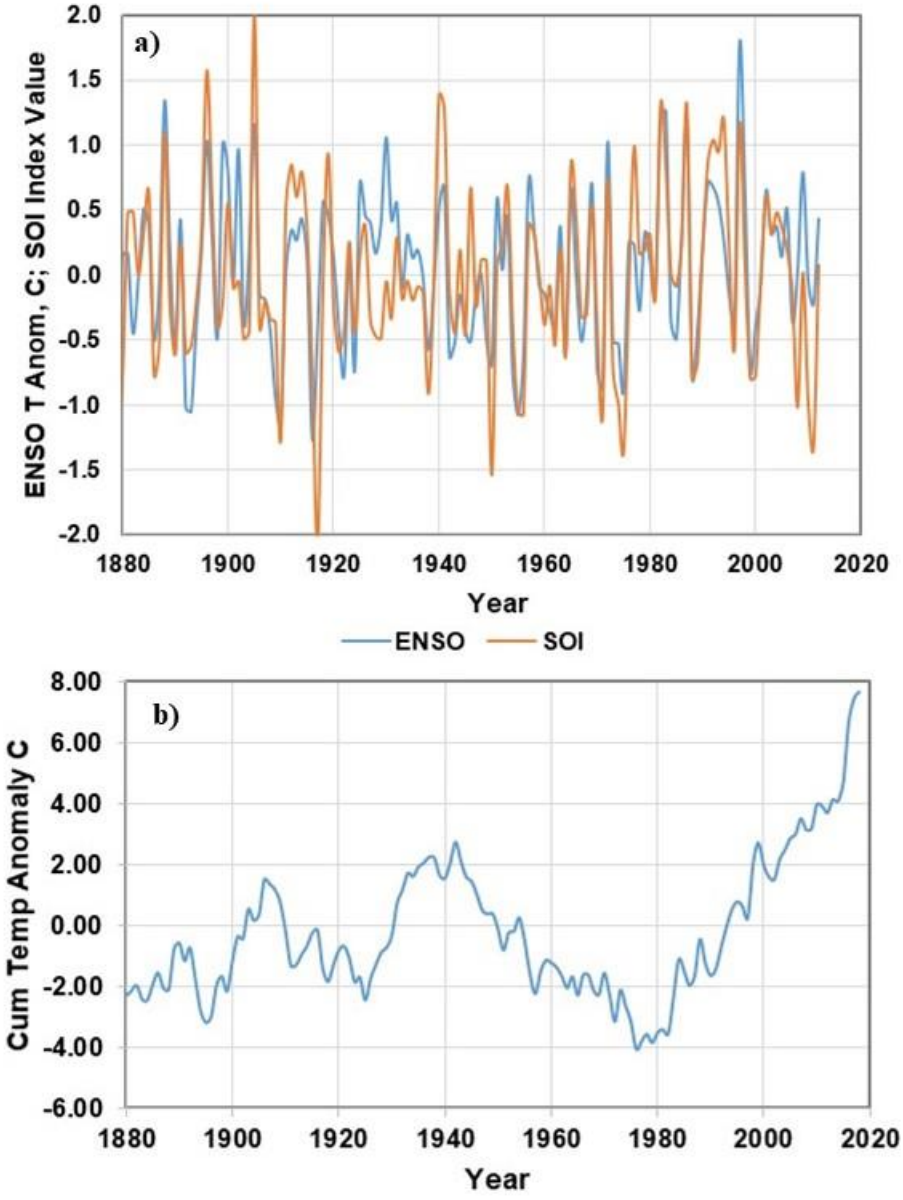

Figure 4: a) ENSO and sign reversed SOI indexes from 1880. There is a clear relationship between temperature and wind speed. b) Cumulative ENSO index (sum over time) showing cooling from 1940 to 1980 and warming from 1980 onwards.

Heat has accumulated at lower depths in the Atlantic and Pacific Ocean basins since 1985 [NOAA, Ocean Heat content, 2019]. The heating of the first 700 m layer is shown in Figure 5. The S. Indian Ocean also exhibits similar behavior. This heat cannot be attributed to any accumulation of LWIR flux from CO_2. Nor does the solar flux penetrate to these depths. Therefore, there is another process that leads to ocean heating and the transport of heat from the surface to lower depths. This requires a more detailed examination of the ocean gyre circulation, in particular, the coupling of the earth's rotation to the wind driven ocean currents. This involves the Coriolis Effect, although in oceanography it is known as Ekman transport and Ekman pumping.

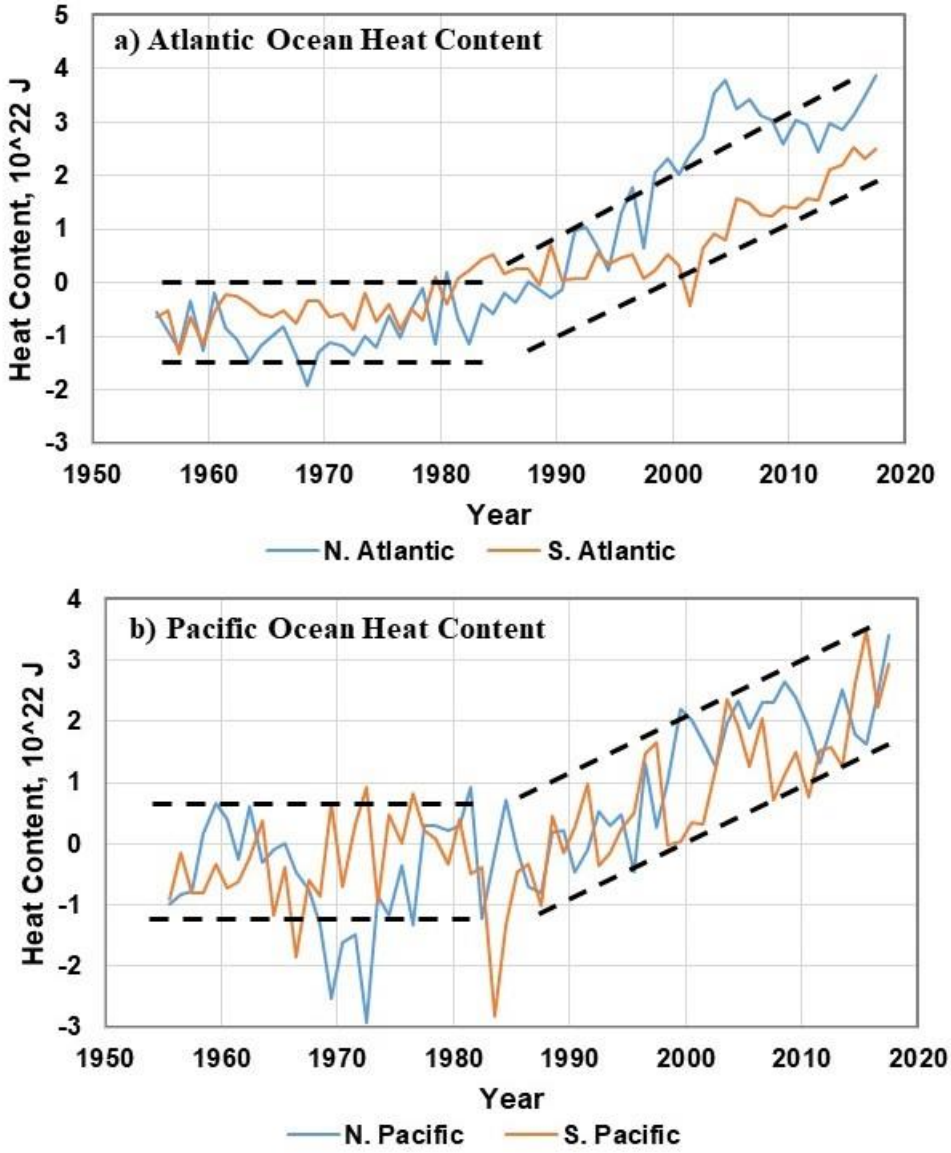

Figure 5: Change in heat content, 0 to 700 m depth, for the N. and S. Atlantic and Pacific Ocean basins from 1955 to 2017. The increase from about 1985 is indicated by the dotted lines.

Ekman Transport and Ekman Pumping

In the oceans, the surface water current flow produced by the wind shear moves at an angle to the wind direction because of the rotation of the earth [NOAA, Ekman Transport, 2019]. In the N. hemisphere, the current moves to the right of the wind direction. Below the surface, the shear continues to drive the current to the right. The direction is reversed in the S. hemisphere. This produces a spiral flow profile in the first 100 to 150 m layer of the ocean. The net flow is at 90° to the wind direction. The circular wind pattern around the ocean gyres produces Ekman pumping. This is illustrated schematically in Figure 6. Within the anticyclonic (high pressure) gyre circulation, Ekman convergence produces downwelling. The depth of the thermocline increases and heat can accumulate below the surface. Along the eastern continental boundary currents,

Ekman divergence produces upwelling. The western continental boundary currents are intensified by the westward equatorial flow and run deeper and faster than the eastern currents. This is illustrated in Figure 7.

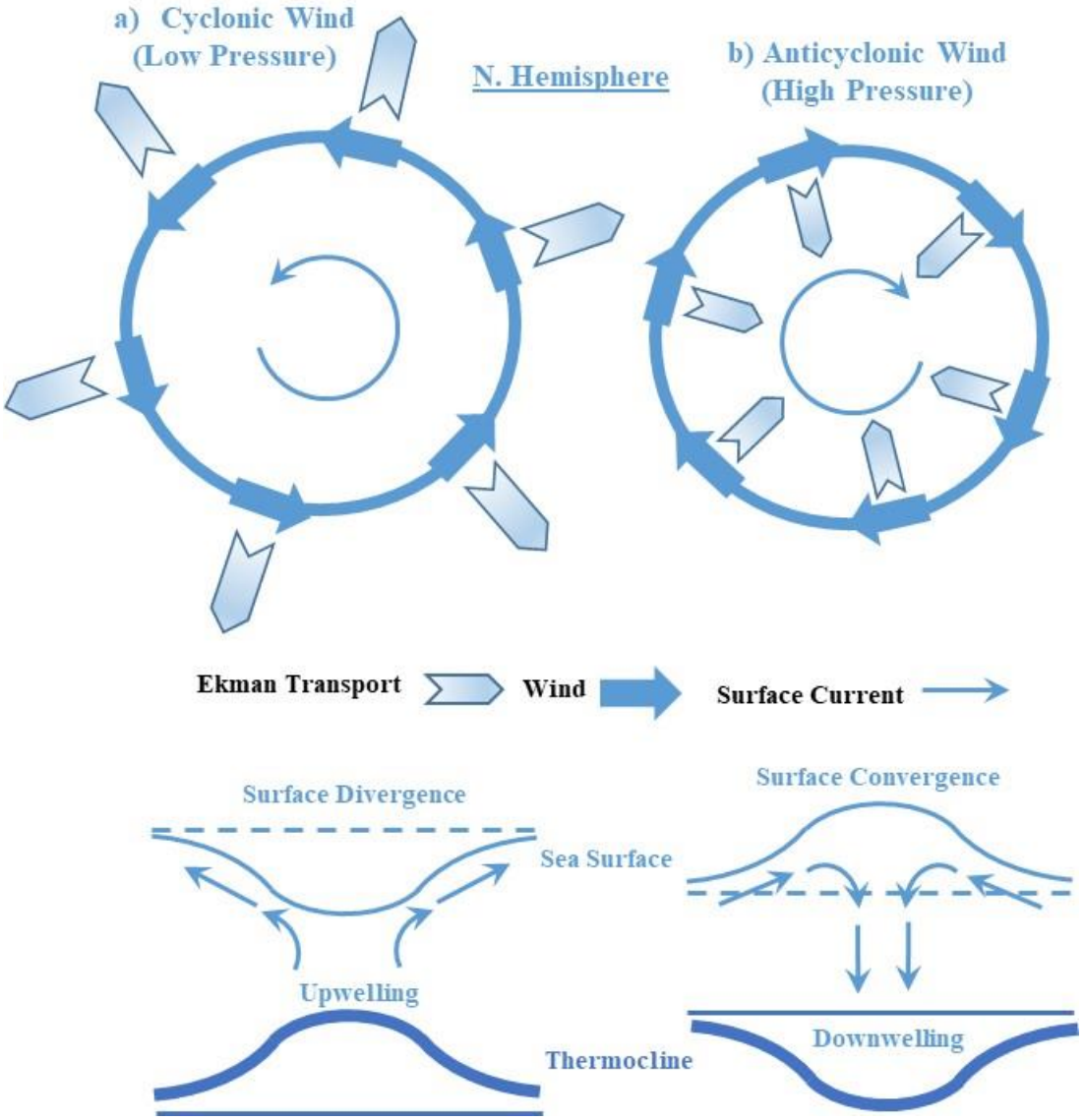

Figure 6: Ekman pumping a) Ekman transport with a cyclonic wind pattern (low pressure) produces surface divergence and upwelling. b) Ekman transport with an anticyclonic wind pattern (high pressure) produces surface convergence and downwelling.

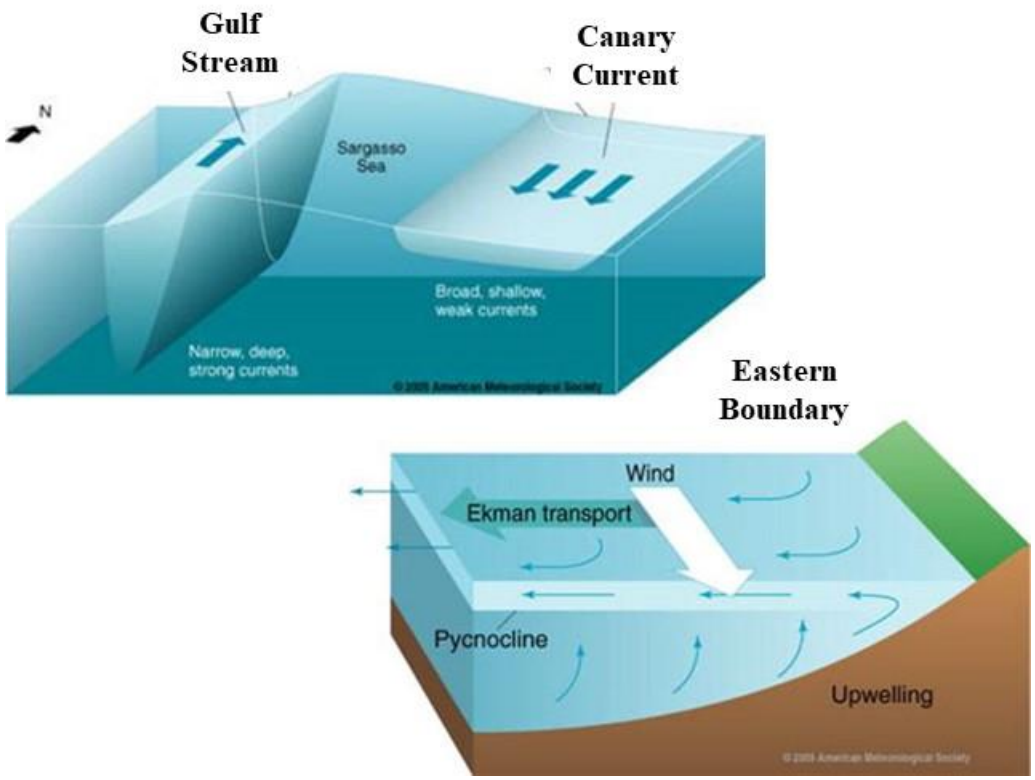

Figure 7: Eastern and western boundary currents (schematic). The eastern boundary current (Canary Current) is wide, slow and shallow. The Ekman transport produces upwelling. The western boundary current (Gulf Stream) is narrow, fast and deep.

Figure 8 shows a set of temperature cross sections of the N. Atlantic Ocean at 10, 20, 30 and 40° N for February and August 2018. These months generally have the lowest and highest temperatures. The plot were generated using the Argo Global Marine Atlas [Argo, 2019]. The color temperature scale changes with the range of temperatures plotted, so the same colors may indicate different temperatures on different plots. Temperature labels have been added for clarity. The cross sections at 10° N are through the N. Atlantic Equatorial current. This flows from E to W towards the W. Atlantic warm pool. Heat accumulates near the surface and the depth of the warm layer increases as the flow moves west. The depth of the 20° C isotherm increase from approximately 50 to 120 m. At 20° N, the isotherms are more widely spaced and the western 18° C isotherm now extends below 300 m. This is the effect of the Ekman convergence within the gyre. At 30° N, the 18 C isotherm extends below 400 m and some of the features associated with the Gulf Stream are beginning to emerge. At 40° N, the meanders of the Gulf Stream are fully developed and the flow is starting to turn eastwards. The Gulf Stream structure extends below 700 m, particularly in February.

The most important point to note however is that wind driven Ekman convergence and the western continental boundary currents are sufficient to transport the surface ocean heat to lower depths. Changes in wind patterns explain the ocean heat gain to 700 m shown in Figure 4. None of the

heat gain in Figure 4 can come from the increase in downward LWIR flux from the observed increase in atmospheric CO_2 concentration.

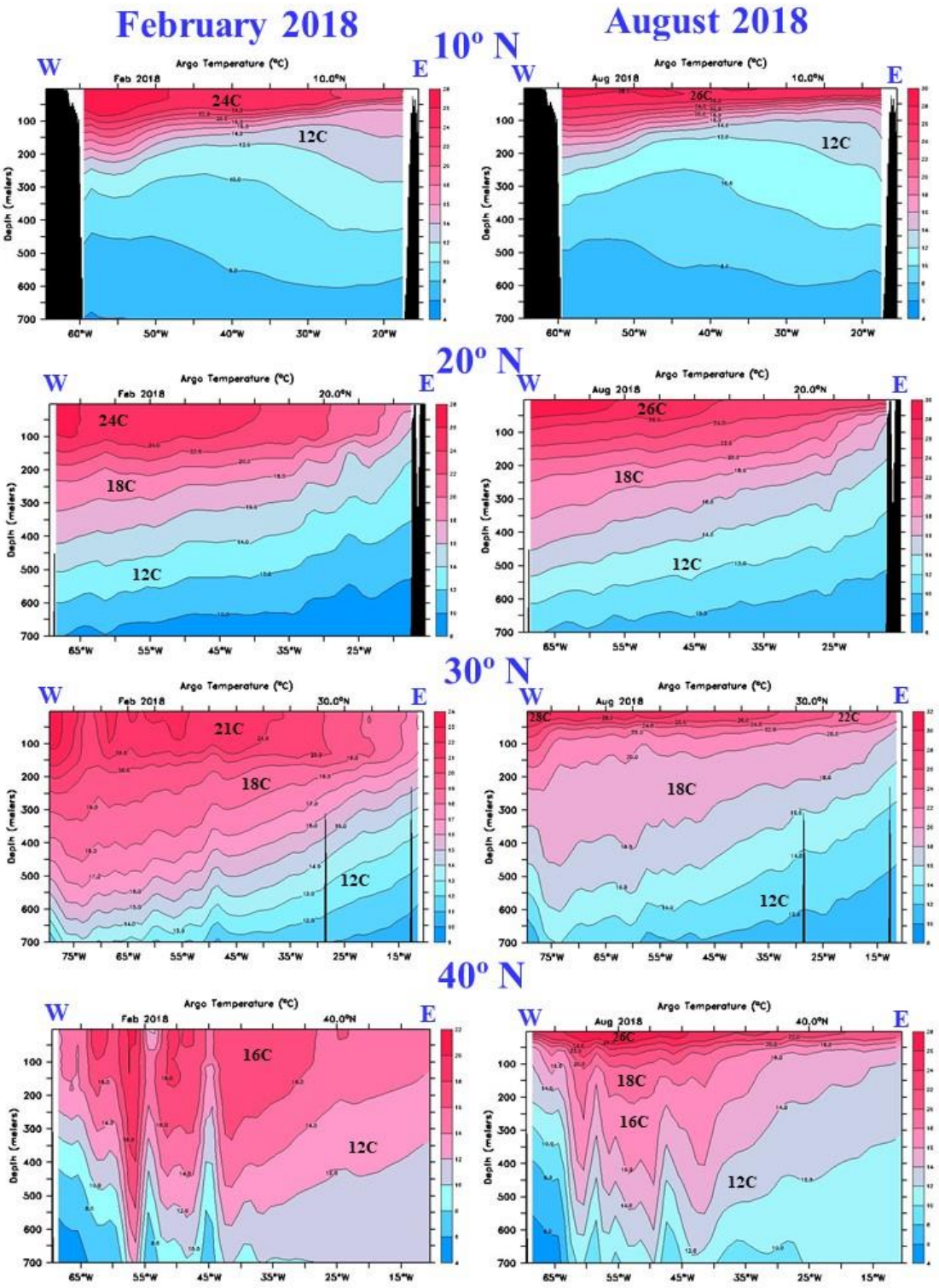

Figure 8: N. Atlantic basin cross sections 0 to 700 m depth at 10, 20, 30 and 40° N showing the isotherms. For discussion see text [plotted from Argo Global Marine Atlas, 2019]

References

Argo, 2019, http://www.argo.ucsd.edu/Marine_Atlas.html
https://www.thegwpf.org/content/uploads/2019/05/JohnChristy-Parliament.pdf

Christy, J. R., GWPF Note 17, 2019, 'The Tropical Skies, Falsifying Climate Alarm',
https://www.thegwpf.org/content/uploads/2019/05/JohnChristy-Parliament.pdf

Clark, R. 2019a, '*A Dynamic Coupled Thermal Reservoir Approach to Atmospheric Energy Transfer Part III: The surface Temperature*', Ventura Photonics Monograph, VPM 004.1, Thousand Oaks, CA, May 2019

http://venturaphotonics.com/files/CoupledThermalReservoir_Part_III_Surface_Temperature.pdf

Clark, R. 2019b, '*A Dynamic Coupled Thermal Reservoir Approach to Atmospheric Energy Transfer Part IV: The Null Hypothesis for CO_2*' Ventura Photonics Monograph, VPM 005.1, Thousand Oaks, CA, May 2019

http://venturaphotonics.com/files/CoupledThermalReservoir_Part_IV_The_Null_Hypothesis.pdf

Clark, R. 2019c, '*A Dynamic Coupled Thermal Reservoir Approach to Atmospheric Energy Transfer Part V: Summary*', Ventura Photonics Monograph, VPM 006, Thousand Oaks, CA, May 2019

http://venturaphotonics.com/files/CoupledThermalReservoir_Part_V_Summary.pdf

Clark, R. 2019d, '*The Greenhouse Effect*', Ventura Photonics Monograph, VPM 003.2, Thousand Oaks, CA, May 2019

http://venturaphotonics.com/files/The_Greenhouse_Effect.pdf

Clark, R. 2019e, '*50 Years of Climate Fraud*', Ventura Photonics Monograph, VPM 002.1, Thousand Oaks, CA, May 2019

http://venturaphotonics.com/files/50_Years_of_Climate_Fraud.pdf

Clark, R., 2013a, Energy and Environment **24**(3, 4) 319-340 (2013), 'A dynamic coupled thermal reservoir approach to atmospheric energy transfer Part I: Concepts'

http://venturaphotonics.com/files/CoupledThermalReservoir_Part_I_E_EDraft.pdf

Clark, R., 2013b, Energy and Environment **24**(3, 4) 341-359 (2013) 'A dynamic coupled thermal reservoir approach to atmospheric energy transfer Part II: Applications'

http://venturaphotonics.com/files/CoupledThermalReservoir_Part_II__E_EDraft.pdf

Clark, R., 2011, *The dynamic greenhouse effect and the climate averaging paradox*, Ventura Photonics Monograph, VPM 001, Thousand Oaks, CA, Amazon, 2011.
https://www.amazon.com/Dynamic-Greenhouse-Climate-Averaging-Paradox/dp/1466359188/ref=sr_1_1?s=books&ie=UTF8&qid=1318571038&sr=1-1

ENSO, 2019, ftp://www.coaps.fsu.edu/pub/JMA_SST_Index/jmasst1868-today.filter-5

Hale, G. M. and Querry, M. R., Applied Optics, **12**(3) 555-563 (1973), 'Optical constants of water in the 200 nm to 200 μm region'

NOAA, 2019, Ekman Transport, http://oceanmotion.org/html/background/ocean-in-motion.htm

NOAA. 2019, Ocean Gyres, https://oceanservice.noaa.gov/facts/gyre.html

NOAA, 2019, Ocean Heat Content, https://www.ncdc.noaa.gov/cdr/oceanic/ocean-heat-content

Ocean-Gyres, 2019, https://oceancurrents.rsmas.miami.edu/ocean-gyres.html

SOI, 2019, ftp://ftp.bom.gov.au/anon/home/ncc/www/sco/soi/soiplaintext.html

UK Met Office, 2017, https://www.metoffice.gov.uk/learning/learn-about-the-weather/how-weather-works/global-circulation-patterns